Research Square

Preprints are preliminary reports that have not undergone peer review.
They should not be considered conclusive, used to inform clinical practice,
or referenced by the media as validated information.

COF-AgNPs Nanoenzymes Combined with Multimodal Machine Learning for Dual-model Detection of Hg 2+ in Aquatic Products

Fuhou Li
Jiangsu Ocean University
Lulu Ye
Jiangsu Ocean University
Jingyi Ye
Jiangsu Ocean University
Zhiwei Xu
Jiangsu Ocean University
Qi Ming
Jiangsu Ocean University
Yumeng Guo
Jiangsu Ocean University
Yachen Wang
Jiangsu Ocean University
Junhuan Wang
Jiangsu Ocean University
Weixia Wang
Jiangsu Ocean University
Jinri Chen
chenjinri@jou.edu.cn
Jiangsu Ocean University

Research Article

Keywords: COF-AgNPs, Colorimetric, Mercury, Machine Learning, Aquatic Products

Posted Date: August 10th, 2026

DOI: https://doi.org/10.21203/rs.3.rs-10206459/v1

License: This work is licensed under a Creative Commons Attribution 4.0 International License.
Read Full License

Additional Declarations: No competing interests reported.

Abstract

Mercury (Hg^{2+}), a highly toxic neurotoxin and carcinogen, endangers the environment and human health even at low exposure. Developing high-performance Hg^{2+} detection is critical for food safety, especially seafood. Herein, a novel silver nanoparticles-based organic framework (COF-AgNPs) nano-enzyme colorimetric sensor combined with multimodal machine learning (ML) for dual-model rapid quantitative detection of Hg^{2+} in aquatic products was developed. The synthesized COF-AgNPs can facilitate the formation of mercury-silver alloys (Hg-Ag) between Hg^{2+} and AgNPs. This combination can significantly enhance the catalytic activity of the nano-enzyme, enabling the generation of the blue oxide 3, 3', 5, 5'-tetramethylbenzidine (oxTMB) from the transparent substance 3, 3', 5, 5'-tetramethylbenzidine (TMB) within 5 min. This COF-AgNPs nano-enzyme sensor addresses the drawbacks of traditional spectroscopic analysis methods, including sophisticated instrumentation, high costs, and lengthy processing times, and can achieve a detection limit of 10.3 nM while exhibiting exceptionally strong anti-interference performance. Meanwhile, to address single-modality limitations and matrix interference, ML was integrated to analyze the detection data. The results show that the support vector machine (SVM) model achieves an accuracy rate of 96.08% in detection, and the developed sensing system is of excellent performance, with a response time of 5 min, visual output, and a wide linear range (0.1–50 μM). By integrating nanozyme sensing technology with ML algorithms, this sensor not only provides an innovative solution for Hg^{2+} detection but also establishes a new paradigm for intelligent sensing systems, enabling its extension to the rapid detection of other heavy metal pollutants.

Introduction

Mercury ions (Hg^{2+}), a globally hazardous pollutant, are particularly dangerous due to their persistence, high toxicity, and ability to bioaccumulate [1, 2]. Hg^{2+} can accumulate in the human body through the food chain and irreversibly bind to sulfur-containing proteins, causing severe pathological effects such as mitochondrial dysfunction, neuronal apoptosis, and Minamata disease [3, 4]. Given the harmful effects of Hg^{2+}, it is necessary to monitor the content of Hg^{2+} in the natural environment and in aquatic products to safeguard food safety and human health.

The existing detection techniques for Hg^{2+}, such as inductively coupled plasma mass spectrometry (ICP-MS), atomic absorption spectroscopy (AAS), and inductively coupled plasma atomic emission spectroscopy (ICP-AES), offer high sensitivity and accuracy [5]. However, these technologies require the use of specialized equipment and personnel with professional skills, which limits their practicality in on-site and real-time detection. In addition, the complex matrix of aquatic products often requires cumbersome pretreatment to reduce signal interference, which is time-consuming and may introduce secondary contamination. Therefore, new detection methods need to be developed to meet the requirements for Hg^{2+} detection.

Recently, nanozymes have shown great potential in analytical sensing due to their high stability, low cost, and easy preparation [6–8]. Their popularity stems from their convenient synthesis, high stability, and low cost [9]. Among various nanozymes, silver-based nanozymes have attracted increasing attention in colorimetric sensing because of their low cost and facile preparation[10, 11]. However, the catalytic stability of the currently commonly used silver-based nano-enzymes is relatively poor, which limits their wider application. To address this issue, researchers have sought to enhance catalytic stability by combining silver nanoparticles (AgNPs) with various organic compounds for Hg^{2+} analysis [12]. Among these organic compounds, covalent organic frameworks (COFs) have shown significant advantages due to their unique structural characteristics. COFs, an emerging class of crystalline porous polymers formed by strong covalent bonds between elements such as carbon (C), nitrogen (N), and oxygen (O), have emerged as ideal carriers for noble metal nanoparticles due to their tunable pore size, high specific surface area, and excellent stability [13]. The strong interactions between their nitrogen-containing groups and nanoparticles not only enhance material stability but also control nanoparticles size through pore confinement effects, thereby improving catalytic activity and sensitivity [14]. Therefore, by combining AgNPs with COFs to prepare a new type of silver-based organic framework nano-enzyme (COF-AgNPs) for Hg^{2+} detection, the sensitivity and stability of the detection can be enhanced [15].

Machine learning (ML) has emerged as a powerful tool for analyzing complex sensing data. It exhibits significant advantages in processing high-dimensional and nonlinear signals, particularly in environments with strong matrix interference such as aquatic products [16, 17]. Traditional nanozyme-based detection methods often rely on single-signal intensity analysis, which is susceptible to interference from matrix components (e.g., proteins, lipids, and minerals in aquatic products) and may lead to deviations in quantitative results. In contrast, ML can integrate multi-dimensional sensing data (including spectral, catalytic kinetic, and morphological characteristic parameters) generated by COF-AgNPs nano-enzymes. By integrating multidimensional sensing data, ML can build robust prediction models that reduce matrix interference and improve the accuracy and specificity of Hg^{2+} detection in complex aquatic-product samples [18, 19].

Herein, a synergistic detection platform integrating COF-AgNPs nanozymes with multimodal ML was constructed for sensitive, rapid, and anti-interference quantification of Hg^{2+} in aquatic products based on the advantages of COF-AgNPs and ML. The Hg^{2+} could promote the COF-AgNPs nanozymes to catalyze the colorless substrate 3, 3', 5, 5'-tetramethylbenzidine (TMB) to change into the blue oxidation state 3, 3', 5, 5'-tetramethylbenzidine (oxTMB). Then the existence of Hg^{2+} was converted to the concentration of oxTMB and the signal was detected by collecting the absorbance data and RGB image information. Furthermore, ML algorithms were employed to process and model the collected sensing data under different data scenarios, optimizing the feature extraction and pattern recognition processes to eliminate matrix interference from aquatic products.

Experiment

Synthesis of COFs and COFs-AgNPs

COFs were synthesized following the procedures described in the literature [20]. A mixture of 14.1 mg TPB and 11.8 mg DVA was dissolved in 5.0 mL ACN containing 2.9 M HAc. The solution was subjected to ultrasonic treatment and reacted at 25 ℃ for 3 d. After the reaction, the COFs was collected by centrifugation and repeatedly washed with tetrahydrofuran and ethanol to remove residual impurities. The cleaned solid was then dried at 50°C for 24 h to obtain a yellow powder. Finally, the as-synthesized COFs were stored at room temperature until further use.

Following the previous report, COF-AgNPs were prepared by in situ reduction to anchor silver nanoparticles (AgNPs) onto the surface of the COFs [21]. The procedure was as follows: 10 mg of COFs were dispersed in 10 mL of anhydrous ethanol and homogenized via ultrasonication. Next, 30 mg of poly (vinylpyrrolidone), 0.5 mL of $AgNO_3$ (0.1 M) solution and 5 mL of ultrapure water, were sequentially added to a conical flask, followed by further ultrasonic dispersion.

0.5 mL of sodium citrate (0.1 M) solution was added and stirred continuously. Subsequently, 0.5 mL of freshly prepared glucose (0.1 M) solution was rapidly introduced under vigorous stirring, and the mixture was stirred for 15 h. After the reaction, the yellow solid product was collected by centrifugation, washed with pure water and methanol, and dried overnight under vacuum.

Detection of Hg

The following colorimetric reaction was carried out to assay Hg^{2+} under the optimal conditions: different concentrations of Hg^{2+} standard solutions were injected into acetate buffer (0.1 M, pH 5.0, 1 mL total volume) containing 200 μL TMB and 50 μL COF-AgNPs (1 mg/mL), followed by reaction at 30°C for 5 min. The absorbance change at 652 nm was then monitored in a 96-well plate using a microplate reader. A standard curve was constructed by correlating the absorbance difference (ΔA_{652}) before and after Hg^{2+} addition with its concentration. Simultaneously, RGB (Red, Green, Blue) color parameters of the reaction system were captured using a smartphone imaging system, and the grayscale value was calculated (grayscale = 0.299R + 0.587G + 0.114B). A quantitative relationship between the grayscale value and Hg^{2+} concentration was ultimately established.

Real sample testing

To evaluate the sensor performance in real samples, five common aquatic products (shrimp, squid, yellow catfish, clams, and kelp) were selected as analytical targets. Sample pretreatment was performed following a reported method with minor modifications [22]. 1 g of each sample was accurately weighed into a conical flask, followed by the addition of 15 mL of nitric acid and 2.5 mL of sulfuric acid. The mixture was allowed to stand overnight at room temperature and then heated to boiling to yield a clear solution. After cooling, the pH was adjusted to 5.0 using 0.1 M NaOH, and the solution was diluted to

100 mL with deionized water. Under optimal conditions, Hg^{2+} standard solutions were spiked into the sample solutions to achieve final concentrations of 5 and 10 μM, respectively. The subsequent detection procedures were identical to those described in “Detection of Hg^{2+}”.

Results and discussion

The Principle of Hg^{2+} Detection

This work developed a novel nano-enzyme colorimetric sensor combined with multimodal ML for rapid detection of Hg^{2+} in aquatic products, which is illustrated in Scheme 1. The working principle includes three parts.

Scheme 1. Schematic illustration of (A) the nanomaterial synthesis route, (B) the Hg^{2+} detection procedure, and (C) the ML processing workflow.

The first part involves the construction of nanozyme COF-AgNPs (Scheme 1A). Firstly, sea urchin-shaped COFs are synthesized by catalyzing TPB and DVA with acetonitrile and acetic acid. Subsequently, COF-AgNPs were prepared by in situ reduction of AgNPs on the COF surface. The obtained COF-AgNPs exhibited enzyme-like catalytic activity.

The second part is the application of nano-enzyme COF-AgNPs in the detection of Hg^{2+} (Scheme 1B). In the presence of Hg^{2+} or mercury compounds, the Ag^{+} in COF-AgNPs can combine with the Hg^{2+} to form an alloy of mercury-silver (Hg-Ag) [23], thereby catalyzes the generation of the blue oxide oxTMB from the colorless substrate TMB [24]. The content of Hg^{2+} can be detected by monitoring the changes in the absorbance and RGB values of the reaction system.

The third part involves using ML to enable computers to automatically "learn" patterns and rules from the actual detected data of Hg^{2+}, and then make predictions or make decisions (Scheme 1C). Firstly, the spectral data and the RGB data collected from the detection samples are preprocessed by using methods such as SG smoothing, SNV, MSC, D1 and D2, etc. to eliminate interference such as instrument noise and optical path differences, so that the data features better match the concentration differences. Secondly, feature dimension reduction and data elimination are carried out to retain the high-discrimination feature data by using methods such as SPA, CARS, and PCA. Thirdly, a dataset is constructed that contains spectral uni-modal data, RGB uni-modal data, and the fused multimodal data of these two types by combining the features. By leveraging the complementarity of absorbance features and RGB features, the classification potential is enhanced. Subsequently, the dataset is divided into training and testing sets in a 7:3 ratio. The obtained training set data is used to train five ML models, namely KNN, SVM, LDA, LR, and RF. Finally, in order to obtain the best training model, multiple indicators such as recall rate, accuracy, precision rate and F1 score are used to evaluate the training results. The optimal model was then used to predict real samples and assess its feasibility for Hg^{2+} detection.

In summary, the presence of Hg^{2+} or mercury compounds leads to the Ag^{+} in COF-AgNPs nano-enzyme combine with the Hg^{2+} to form Hg-Ag, which catalyzes the generation of the blue oxidized product oxTMB from the colorless substrate TMB, thereby a COF-AgNPs-based nano-enzyme colorimetric sensor coupled with multimodal ML for rapid, accurate dual-model detection of Hg^{2+} in aquatic products is developed.

Characterization of COFs

The successful synthesis of COFs has a significant impact on the synthesis of the nanozyme COF-AgNPs. Therefore, it is necessary to conduct material characterization of COFs.

The preparation process of COFs is illustrated in Fig. S2. DVA and TPB are as monomers to self-assemble a nitrogen-rich COF backbone via a room-temperature Schiff base reaction for 72 h.

Primarily, the morphology and size of COFs were characterized by SEM and TEM, and the results are shown in Fig. S3A and Fig. S3B. The results show that in the SEM image, the COFs present as aggregated petal-like structures. Under TEM, the COFs exhibit complete sea urchin-like shapes, with particle sizes spanning 390 to 400 nm and an average particle diameter of 398.21 nm.

Secondly, the chemical composition of COFs was characterized by XPS, and the results are shown in Fig. S3C and Fig. S3D.

The full XPS spectrum of the COFs exhibits three characteristic peaks (Fig. S3C). The C, N and O in COFs are indicated as C 1s (281 eV), N 1s (396 eV) and O 1s (529 eV), respectively. The results indicate that the composition of the COFs is close to that of TPB and DVA molecules.

C 1s spectrum analysis of COFs shows that there are two peaks of C = C/C = N (284.78 eV) and C–O (286.3 eV) (Fig. S3D). The presence of the C = N bond peak at 284.78 eV provides direct evidence for the successful formation of the COFs via the Schiff base condensation reaction.

Afterwards, FTIR was used to monitor the evolution of functional groups during the synthesis of COFs (Fig. S3E). In the TPB monomer, N–H stretching vibrations at 3434 cm^{-1} and 3354 cm^{-1} are significantly weakened or absent in the COFs spectrum. Similarly, in the DVA monomer, the saturated C–H stretching peak at 2869 cm^{-1} and the aldehyde C = O characteristic peak at 1681 cm^{-1} also exhibit a marked weakening or disappearance. Concurrently, a new strong absorption peak at 1592 cm^{-1} appeared in the COFs spectrum, which is assigned to the C = N stretching vibration. These spectral changes confirm that TPB and DVA successfully formed the COFs via a typical Schiff base condensation reaction ($–CHO + –NH_2 \rightarrow –C = N– + H_2O$).

Finally, the COFs were characterized by XRD, as shown in Fig. S3F. The XRD spectra of COFs reveals clear characteristic diffraction peaks at 5.51°, 7.34°, 9.62°, and 25.2° for the COFs, which are consistent with

the crystal structure reported by Ma et al. [20].

From the above characterization results, it can be concluded that the COFs have been successfully synthesized.

Characterization and selectivity of COF-AgNPs

The successful synthesis of nano-enzyme COF-AgNPs is crucial for determining the feasibility of the Hg^{2+} detection principle. Therefore, it is necessary to conduct characterization on the nano-enzyme COF-AgNPs.

The preparation process of COF-AgNPs is illustrated in Fig. 1A. The solid powder of COFs is dissolved in anhydrous ethanol. Subsequently, PVP, ultrapure water, and $AgNO_3$ are added sequentially. After the resultant mixture has undergone sufficient reaction, sodium citrate is introduced. Lastly, an aqueous glucose solution is rapidly injected under vigorous magnetic stirring.

To verify whether the COF-AgNPs were successfully synthesized, experiments such as SEM, TEM, XPS, XRD, FTIR, energy-dispersive X-ray spectroscopy (EDS), and Zeta potential analysis were carried out.

First of all, the morphology and size of COF-AgNPs were characterized by SEM and TEM, and the results are shown in Fig. 1B and Fig. 1C. The results show that COF-AgNPs retain the basic morphology of COFs, and their particle size ranges from 500 to 550 nm, which is larger than the particle size of COFs (390 to 400 nm). Additionally, the difference is that COF-AgNPs have a shape more resembling a spherical structure under SEM imaging, and the average particle size shown under TEM is 525.87 nm.

Secondly, the chemical composition of COF-AgNPs was characterized by XPS and EDS, and the results are shown in Fig. 1D, Fig. S4 and Fig. S5.

The complete XPS spectrum of COF-AgNPs has five characteristic peaks (Fig. 1D). The C, N, O, and Ag are represented in COF-AgNPs as C 1s (281 eV), N 1s (396 eV), O 1s (529 eV), and Ag 3d (368.49 eV and 374.51 eV), respectively.

Figure 1. (A) SEM image of COF-AgNPs; (B) TEM image and particle size distribution of COF-AgNPs (inset); (C) XPS full spectra of COF-AgNPs; (D) High-resolution XPS spectra of Ag3d in COF-AgNPs; (E) UV-Vis absorption spectra and corresponding solution photographs of COFs, AgNPs, COF-AgNPs reacted with TMB in the presence/absence of Hg^{2+} (inset); (F) Zeta potential distribution of COFs, COFs + Hg^{2+}, COF-AgNPs and COF-AgNPs + Hg^{2+}.

The results suggest that the composition of the COF-AgNPs is close to that of COFs and $AgNO_3$.

C 1s spectrum analysis of COF-AgNPs shows that there are three peaks of C = C/C = N (284.78 eV), C–O (286.1 eV) and O-C = O(288.3 eV) (Fig. S4A). The C = N bond peak observed at 284.78 eV indicates that

the COF-AgNPs also possess the same organic framework as the COFs.

O 1s spectrum analysis of COF-AgNPs reveals that there are two peaks of -OH (531.52 eV) and C–O (533.12 eV) (Fig. S4B).

The new O-C = O bond peak in the C 1s spectrum of COF-AgNPs and the new -OH peak in its O 1s spectrum primarily originated from the sodium citrate stabilizer and glucose reducing agent used during the synthesis.

N 1s spectrum analysis of COF-AgNPs shows that there is a new peak at 402.86 eV is detected for COF-AgNPs (Fig. S4C), which is attributed to Ag-N bonds and provides direct evidence for the chemical anchoring of AgNPs on the COFs surface [25].

In the high-resolution Ag 3d spectrum (Fig. 1E), the binding energies of Ag $3d_{5/2}$ and Ag $3d_{3/2}$ are 368.49 eV and 374.51 eV, respectively, with a standard separation energy of 6.02 eV [21]. This binding energy profile matches the characteristic energy of metallic silver (Ag^0), further confirming the successful loading of AgNPs onto the COFs surface.

Elemental mapping analysis via EDS (Fig. S5) confirmed the uniform distribution of C, N, O, and Ag elements throughout the composites [21]. Notably, the spatial distribution of Ag elements closely matched the morphology of the COFs substrates, providing direct evidence for the successful loading of AgNPs.

Subsequently, FTIR was used to monitor the evolution of functional groups during the synthesis of COF-AgNPs. As show in Fig. S3E, COF-AgNPs retain the characteristic C = N peak at 1592 cm^{-1}, and the spectrum show high similarity to that of pristine COFs, which is proved that AgNP loading does not disrupt the imine bond framework structure of the COFs.

Finally, the COF-AgNPs were characterized by XRD, and the results are shown in Fig. S3F. The XRD spectra of COF-AgNPs exhibits new characteristic diffraction peaks at 38.24° and 44.15° compared to those of pristine COFs, which correspond to the (111) and (200) planes of face-centered cubic AgNPs, thereby confirming the presence of crystalline AgNPs.

Based on the above characterization results, it is proved that COF-AgNPs have been successfully synthesized.

After successfully obtaining the nano-enzyme COF-AgNPs, the selectivity of this nano-enzyme needs to be characterized. This work investigated the feasibility of the nano-enzyme sensor for detecting Hg^{2+} through absorbance curves, Zeta potential analysis and TEM characterization.

As illustrated in Fig. 1F, the ultraviolet absorption spectra curves a, b, c and d correspond to COFs, COFs + Hg^{2+}, COF-AgNPs, and COF-AgNPs + Hg^{2+}, respectively. When there is no Hg^{2+}, the absorbance value of the solution is low, and the solution appeared light yellow to the naked eye (Fig. 1F, curves a and c). This

result indicates that in the absence of Hg^{2+}, COFs and COF-AgNPs alone cannot trigger the reaction of the colorless substrate TMB, resulting in the formation of the blue oxide oxTMB.

Furthermore, even when Hg^{2+} is present, the absorbance value of the solution is relatively low, and the solution still appears light yellow to the naked eye (Fig. 1F, curve b). This result indicates that even in the presence of Hg^{2+}, COFs are unable to catalyze the generation of the blue oxidized product oxTMB from the colorless substrate TMB.

Conversely, the presence of Hg^{2+} results in a marked increase in absorbance of the reaction system at 652 nm and a noticeable blue coloration of the solution when observed visually (Fig. 1F, curve d). This result indicates that in the presence of Hg^{2+}, the nano-enzyme COF-AgNPs can catalyze the generation of the blue oxidized product oxTMB from the colorless substrate TMB, suggesting that COF-AgNPs have selectivity.

Subsequently, the charge differences among the charge differences among COFs, COFs + Hg^{2+}, COF-AgNPs and COF-AgNPs + Hg^{2+} were analyzed via Zeta potential measurements were analyzed via Zeta potential measurements (Fig. 1G).

The Zeta potential of COF-AgNPs was − 31.8 mV, indicating a markedly enhanced negative charge compared with that of pristine COFs (-19.1 mV). According to the colloidal stability theory, the absolute value of this potential exceeding 30 mV attests to the excellent dispersion stability of COF-AgNPs, which is attributed to the strengthened electrostatic repulsion that effectively inhibits nanoparticle agglomeration [26]. Furthermore, the enhanced negative charge improves the material's affinity for positively charged substrates through electrostatic attraction, thereby optimizing its catalytic performance. Upon introducing Hg^{2+} into both material systems, the Zeta potential underwent a directional reversal: the potential of COF + Hg^{2+} shifted from − 19.1 mV to 13.1 mV, while that of COF-AgNPs + Hg^{2+} shifted from − 31.8 mV to 19.4 mV. This phenomenon confirms that Hg^{2+} can specifically bind to the functional groups on the material surface, neutralizing negative charges and imparting positive surface charge via charge rearrangement. Moreover, the larger positive potential shift of COF-AgNPs reflects its superior targeted binding ability toward Hg^{2+}.

Finally, the results from the TEM image show that when Hg^{2+} is present, Hg^{2+} causes the aggregation of the nano-enzyme COF-AgNPs, indirectly proving that the Ag^{+} of COF-AgNPs combine with Hg^{2+} to form an alloy of mercury-silver (Hg-Ag) (Fig. S6).

Additionally, the enzymatic activity of COF-AgNPs was investigated through steady-state kinetic analysis. As shown in Fig. S7A and Fig. S7B, Hg^{2+} can reduce the Michaelis constant (k_m) of COF-AgNPs from 0.642 mM to 0.366 mM, and increase the maximum reaction rate (v_{max}) to 10.722×10^{-8} $M\cdot s^{-1}$ These results demonstrate that the presence of Hg^{2+} has simultaneously enhanced the affinity and catalytic efficiency of COF-AgNPs towards the substrate. It is noteworthy that, compared with previously reported

silver-based nanoenzymes (Table S1), COF-AgNPs and their mercury-ion-modified variants exhibit lower k_m values in the TMB reaction. These results clearly indicate that Hg^{2+} significantly enhance the oxidase-like activity of COF-AgNPs, manifested as the simultaneous improvement of affinity and catalytic efficiency towards the substrate. This discovery provides crucial evidence for understanding the specific catalytic mechanism of nano-enzyme COF-AgNPs.

Meanwhile, to explore the catalytic reaction mechanism of the nano-enzyme COF-AgNPs, the role of reactive oxygen species (ROS) during the oxidation process was also investigated (Fig. S7C). As can be seen from Fig. S7C, isopropyl alcohol (IPA) was added to the catalytic system (COF-AgNPs + Hg^{2+}) caused only minor changes in absorbance, suggesting a minimal contribution from hydroxyl radicals (·OH). However, both the histidine (His)-treated and *p*-benzoquinone (*p*-BQ)-treated exhibited significant absorbance decreases, confirming the generation of singlet oxygen ($^1O_2$) and superoxide anion radicals ($\cdot O^{2-}$) in the system. The pronounced inhibitory effect in the *p*-BQ group clearly indicates that $\cdot O^{2-}$ plays a key role in TMB oxidation, which is consistent with the dominant role of superoxide radicals in typical oxidase catalytic mechanisms [27].

Based on the above feasibility verification results, it is proved that the use of nano-enzyme COF-AgNPs for the detection of Hg^{2+} is completely feasible.

Optimization of experimental conditions

To achieve the best detection effect of the nano-enzyme COF-AgNPs, it is necessary to optimize the parameters such as reaction temperature, reaction time, the amount of nano-enzyme, the pH value of the reaction system, and the amount of TMB.

During optimization, the absorbance value was used as an index to represent the detection effect of nano-enzyme COF-AgNPs. As shown in Fig. S8A, the absorbance value of this nano-enzyme COF-AgNPs sensor begins to increase significantly at a reaction temperature of 30°C, and then decrease as the temperature increase. Therefore, 37°C is the optimal reaction temperature. Subsequently, the reaction time of nano-enzyme COF-AgNPs was optimized. As shown in Fig. S8B, the absorbance value of this nano-enzyme COF-AgNPs sensor begins to increase significantly as the reaction time increases. After 5 min of reaction time, the absorbance no longer increases, so the optimal reaction time is 5 min.

After the optimal reaction temperature and time were determined, the dosage of COF-AgNPs was also studied. As shown in Fig. S8C, the absorbance value of this nano-enzyme COF-AgNPs sensor reaches its peak when the concentration of COF-AgNPs is 1.0 mg/mL, so the optimal dosage of COF-AgNPs is 1.0 mg/mL.

Subsequently, the pH value of the reaction system and the amount of TMB were optimized. As shown in Fig. S8D and Fig. S8E, the absorbance value of this nano-enzyme COF-AgNPs sensor begins to increase significantly at a pH value of 5.0, and then decrease as the pH value of the reaction system. Therefore,

pH 5.0 is the optimal pH value of the reaction system. And the absorbance value of this nano-enzyme COF-AgNPs sensor reaches its peak when the TMB substrate amount is 0.7 mM, so the TMB substrate amount is 0.7 mM.

Establishment of COF-AgNPs nano-enzyme sensor for Hg^{2+}

Under optimized experimental conditions, the sensitivity of nano-enzyme COF-AgNPs in detecting Hg^{2+} was investigated. The COF-AgNPs nano-enzyme sensor for colorimetric detection of Hg^{2+} has two modes: the detection mode based on absorbance value and the detection mode based on RGB value.

Experimental results show that as Hg^{2+} concentration increases (0–50 μM), the characteristic absorption peak at 652 nm significantly intensifies (Fig. 2A). The solution color gradually shifts from light blue to dark blue, visually indicating changes in Hg^{2+} concentration. Quantitative analysis revealed that there were two excellent linear relationships ($R^2 > 0.99$) between ΔA_{652} and Hg^{2+} concentration across two ranges: 0.05–0.5 μM and 5–50 μM (Fig. 2B and Fig. 2C), with linear regression equations of $Y = 0.4398*c(Hg^{2+}) - 0.03468$ and $Y = 0.0217*c(Hg^{2+}) + 0.2958$, respectively. The calculated limit of detection (LOD) for Hg^{2+} is 10.3 nM (signal-to-noise ratio, S/N = 3), indicating its extremely high sensitivity.

Compared with other existing nanocatalyst-based colorimetric methods, this approach shows distinct advantages, including a lower detection limit and broader linear range (Table S2), indicating high sensitivity and suitability for Hg^{2+} detection in aquatic products.

To further simplify Hg^{2+} detection, a smartphone-based colorimetric analysis platform was developed. Under standardized illumination conditions, colorimetric images of the reaction system were captured using the smartphone's rear camera at a fixed distance and angle (Fig. 2D). The built-in Picker Color application precisely extracted RGB color parameters from each reaction well, converting color signals into quantitative data via the algorithm Gray = 0.299R + 0.587G + 0.114B. As shown in Fig. 2E and Fig. 2F, this intelligent detection system exhibits an excellent linear response within the 0.5–15 μM concentration range. The corresponding quantitative model is Gray = -3.29323c + 153.1088 ($R^2 = 0.995$), with a LOD of 1.32 μM (S/N = 3), confirming the reliability of the smartphone-based detection platform.

Figure 2. (A) UV-Vis absorption spectra (500–800 nm) as a function of Hg^{2+} concentrations (inset: photographs of the colorimetric reaction); (B) Linear calibration curve for Hg^{2+} detection by microplate reader (linear range: 0.05–0.5 μM); (C) Linear calibration curve for Hg^{2+} detection by microplate reader (linear range: 5–50 μM); (D) RGB values as a function of Hg^{2+} concentrations obtained by smartphone analysis (inset: photographs of color development); (E) Grayscale intensity profile as a function of Hg^{2+} concentrations; (F) Linear calibration curve for Hg^{2+} detection based on RGB values.

High selectivity is crucial for the detection of Hg^{2+} in real samples, as it determines whether the method can be effectively applied to practical sample analysis. Even after digestion treatment, the seafood samples may still contain various metal ions. These ions may interfere with the selectivity of Hg^{2+} detection. Therefore, common metal ions and anions in seafood (Al^{3+}, Pb^{2+}, Mg^{2+}, Cd^{2+}, Ca^{2+}, Mn^{2+}, SO_4^{2-}, CO_3^{2-}, Cl^-, PO_4^{3-}, K^+, Zn^{2+}, Na^+, Ni^{4+}, Cu^{2+}) were selected for selectivity testing. The concentrations of metal ions and other ions such as anions were set at 10 times that of Hg^{2+}. Under the optimal conditions for Hg^{2+} detection, different metal ions were individually added to the same system, and the absorbance values at 652 nm were measured using a microplate reader. As shown in Fig. 3A, apart from Hg^{2+}, the responses of other ions to this COF-AgNPs nano-enzyme sensor were negligible, indicating that this method exhibits high specificity for Hg^{2+} detection and is not significantly affected by other ions.

To evaluate the long-term stability of COF-AgNPs, the changes in their nanozyme performance for detecting Hg^{2+} over a 7 d storage period were systematically investigated. As shown in Fig. 3B, using the enhanced absorbance change by Hg^{2+} as the evaluation metric, the COF-AgNPs retained over 90% of their initial enzymatic activity after 7 d of storage. This result demonstrates that COF-AgNPs maintain high enzymatic activity and stability even after prolonged storage.

Figure 3. (A) Effects of common metal cations and anions on the absorbance response for Hg^{2+} detection; (B) Time-dependent (7 days) enhancement of oxidase-like activity in COF-AgNPs induced by Hg^{2+}.

Detection of Hg^{2+} in real samples

To demonstrate the feasibility of this COF-AgNPs nano-enzyme sensor in analytical applications, five representative seafood samples (shrimp, squid, yellow catfish, clams, and kelp) were selected to evaluate the analytical performance of the proposed method. The recovery rates were calculated based on the established standard curves, with all experiments repeated three times.

As shown in Table 1, the recovery rates ranged from 90.18% to 103.22%, with relative standard deviations (RSD) between 0.9% and 8.87%. These results indicate that the colorimetric detection method utilizing Hg^{2+}-enhanced COF-AgNPs oxidase activity is feasible and reliable, demonstrating satisfactory accuracy and precision with broad application potential.

Table 1

Detection of Hg^{2+} in real samples.

Samples	method	Added (μM)	Detected (μM)	Recovery (%)	RSD (%,n = 3)
Shrimp	Absorbance	5	4.98	99.63	3.59
		10	9.55	95.45	0.92
	RGB	5	5.00	100.04	7.87
		10	10.32	103.22	4.65
Yellow catfish	Absorbance	5	4.82	96.34	4.25
		10	9.74	97.36	4.82
	RGB	5	4.96	99.11	7.02
		10	9.78	97.75	1.36
Clams	Absorbance	5	4.73	94.53	1.68
		10	9.71	97.10	3.84
	RGB	5	4.51	90.19	8.87
		10	9.82	98.23	6.47
Squid	Absorbance	5	4.86	97.14	2.63
		10	10.03	100.32	1.28
	RGB	5	5.11	102.21	5.41
		10	9.53	95.33	4.48
Kelp	Absorbance	5	4.91	98.19	1.90
		10	10.04	100.40	3.28
	RGB	5	4.66	93.28	7.10
		10	9.59	95.85	6.02

Multimodal ML for High-Precision Hg^{2+} Detection

To facilitate the accurate and timely processing of experimental data from this COF-AgNPs nano-enzyme sensor, as well as to realize the functions of prediction, classification, and optimization, it is necessary to select an appropriate mathematical model (Fig. S9).

As shown in Fig. S9A, the results showed that MSC significantly reduced signal noise and baseline drift, yielding the optimal classification accuracy, precision, recall, and F1-score, thus providing high-quality data support for subsequent modeling.

In the feature extraction stage (Fig. S9B), CARS was compared with raw spectral features, SPA and PCA, CARS effectively selected discriminative features strongly correlated with Hg^{2+} concentration, which significantly reduced model redundancy and improved classification efficiency.

During model selection, spectral features, RGB features, and their fusion features were input into KNN, LDA, LR, RF and SVM models. This COF-AgNPs nano-enzyme sensor reliability was validated by assessing the detection performance of each model across low, medium, and high Hg^{2+} concentrations. Comprehensive comparisons of classification performance across different models (Fig. S9C) and modalities (Fig. S9D) revealed that the spectral-color fusion dataset yielded superior performance in the KNN, RF, and SVM models, with over a 10% improvement compared to single-spectral models. SHapley Additive exPlanations (SHAP) interpretability analysis (Fig. S10) further validated that the synergistic interaction between absorbance and RGB channel values dominates prediction outcomes, providing quantitative evidence for the multimodal sensor data fusion mechanisms.

Subsequently, a systematic evaluation was performed to assess the detection performance of different ML models for low-, medium-, and high-concentration Hg^{2+}. As shown in Fig. 4A, KNN, RF, and SVM all demonstrated superior classification performance for both low and high concentration samples. Comprehensive performance comparison (Fig. 4B) revealed that the SVM outperformed the other models overall, followed closely by RF and KNN.

An in-depth analysis of the SVM model revealed the following: the confusion matrix (Fig. 4C) showed minimal classification errors across samples with different Hg^{2+} concentrations, achieving an overall accuracy of 95.3%. ROC (Fig. 4D) curves indicated area under the curve (AUC) values of 0.99, 0.96, and 0.97 for the three sample categories, reflecting excellent generalization ability. In the fitting analysis of predicted versus actual values (Fig. 4E), the coefficient of determination (R^2) approached 1 and the root mean square error (RMSE) was extremely low, demonstrating excellent quantitative prediction accuracy. In the testing of actual samples (Fig. 4F), a correlation analysis between predicted and measured values (R^2 = 0.994) showed that the model exhibited a strong linear correlation when predicting Hg^{2+} concentrations in real samples. It also demonstrated excellent quantitative detection accuracy and stability, thereby supporting the precise analysis of actual samples.

Through multi-stage ML optimization, the detection range was expanded from the traditional segmented or narrow intervals to a continuous linear range of 0.01-50 μM. Specifically, the low concentration detection limit was reduced to 0.01 μM, which meets the requirements of trace detection. The upper detection limit was maintained at 50 μM, exceeding the 15 μM limitation of RGB signals and thus adapting to microanalysis scenarios. This optimization eliminates the fragmented detection range of traditional systems, significantly expanding the dynamic detection range. Consequently, it provides comprehensive technical support for the precise and continuous detection of Hg^{2+} across different concentration gradients.

Figure 4. (A) Performance comparison of machine learning models across low, medium, and high concentration ranges; (B) Overall performance benchmarking of ML models; (C) Visualization results of the confusion matrix for the decision tree model; (D) ROC curve of the decision tree model and corresponding area under the curve (AUC) analysis; (E) Regression scatter plot of the model prediction values versus actual measured values, along with error distribution; (F) Linear regression plot of the model prediction values versus actual measured values in practical samples.

Conclusions

In conclusion, this study presents a novel COF-AgNPs nano-enzyme colorimetric sensor combined with multi-modal ML for dual-model rapid detection of Hg^{2+} in aquatic products. The characteristic of the COF-AgNPs nano-enzyme sensor is that AgNPs combine with Hg^{2+} to form an alloy of silver and mercury. This combination significantly enhances the catalytic activity of the nano-enzyme, enabling it to catalyze the generation of the blue oxidized product oxTMB from the colorless substrate TMB within 5 min. And this COF-AgNPs nano-enzyme sensor overcomes the limitations of traditional spectroscopic analysis methods, such as complex equipment, high costs, and long processing times. It achieves a LOD of 10.3 nM and exhibits extremely strong anti-interference ability. Meanwhile, in order to enhance the sensitivity of the detection and achieve functions such as prediction, classification and optimization, ML methods were employed to analyze the detection data. The results showed that the SVM model could achieve an accuracy rate of 96.08% in the detection, which was a significant improvement compared to the traditional colorimetric method. The developed sensing system offers outstanding performance with a 5 min response time, visual output, and a broad linear range of 0.1–50 μM, fully meeting the technical requirements for on-site rapid detection in fields such as food safety regulation. This strategy combining nanozyme sensing with machine learning algorithms not only enriches the methodological system for Hg^{2+} detection, but also provides a new approach for the construction of intelligent sensing platforms, demonstrating great potential in the rapid monitoring of other heavy metal pollutants.

Declarations

Declaration of Competing Interest

The authors declare no conflicts of interest.

Artificial Intelligence Disclosure Statement

ChatGPT (GPT-4o, OpenAI) was used solely for English linguistic revision of this manuscript. No AI tools were involved in research design, data processing, figure drawing or result analysis. All figures were manually drawn by the authors, and all scientific content was independently generated and verified by the authors.

COF-AgNPs Nanoenzymes Combined with Multimodal Machine Learning for Dual-model Detection of Hg^{2+} in Aquatic Products

Fuhou Li[a, c, d, 1], Lulu Ye[a, c, d, 1], Jingyi Ye[a, c, d], Zhiwei Xu[a, c, d], Qi Ming[a, c, d], Yumeng Guo[a, c, d], Yachen Wang[a, c, d], Junhuan Wang[a, c, d], Weixia Wang[a, c, d], Jinri Chen[a, b, c, d, *]

Author Contribution

Fuhou Li: Conceptualization, Methodology, Visualization, Resources, Writing original draft & editing. Lulu Ye: Conceptualization, Methodology, Investigation, Writing original draft & editing, Visualization. Jingyi Ye: Methodology, Investigation, Formal analysis, Visualization. Zhiwei Xu: Investigation, Methodology, Data curation. Qi Ming: Investigation, Methodology, Formal analysis. Yumeng Guo: Investigation, Methodology, Formal analysis. Yachen Wang: Data curation, Formal analysis, Visualization. Junhuan Wang: Methodology, Validation. Weixia Wang: Investigation, Methodology, Formal analysis. Jinri Chen: Conceptualization, Writing-review & editing, Supervision, Visualization, Project administration, Funding acquisition.

Acknowledgements

This work was financially supported by China Postdoctoral Science Foundation (2023M731397), Lianyungang Postdoctoral Research Funding Program (LYG20230015), and the Natural Science Foundation of Jiangsu Ocean University (KQ23020).

References

1. Garg N, Shukla P, Mullapudi VBK (2026) Toxic legacy of mercury: From contamination pathways, exposure risks to remediation technologies. J Environ Chem Eng 14:120600. https://doi.org/10.1016/j.jece.2025.120600
2. Jomova K, Alomar SY, Nepovimova E et al (2025) Heavy metals: toxicity and human health effects. Arch Toxicol 99:153–209. https://doi.org/10.1007/s00204-024-03903-2
3. Li SY, Li ZR, Wu MJ, Zhou Y, Tang WL, Zhou H (2024) Mercury transformations in algae, plants, and animals: The occurrence, mechanisms, and gaps. Sci Total Environ 911:168690. https://doi.org/10.1016/j.scitotenv.2023.168690
4. Luo XQ, Yang PJ, Tian XW, Guo YY, Shen ZL, Liu YW, Li YB, Zhang QH, Song MY, Yin YG, Cai Y, Jiang GB (2025) Particulate mercury (Hg) dominates the microbially available Hg pool over dissolved Hg during the decay of marine diatom Chaetoceros debilis. J Hazard Mater 494:138602. https://doi.org/10.1016/j.jhazmat.2025.138602

5. Sarkar DJ, Behera BK, Parida PK, Aralappan VK, Mondal S, Dei J, Das BK, Mukherjee S, Pal S, Weerathunge P, Ramanathan R, Bansal V (2023) Aptamer-based NanoBioSensors for seafood safety. Biosens Bioelectron 219:114771. https://doi.org/10.1016/j.bios.2022.114771
6. Wu J, Zhang T, Jia X, Li JX, Xie HJ, Yan F, Li DW, Liu JY (2026) Mesoporous vanadium-doped Fe_3O_4 nanozymes with enhanced peroxidase-mimetic activity for colorimetric/electrochemical dual-mode detection of nitrite in food and seawater samples. J Colloid Interface Sci 701:138721. https://doi.org/10.1016/j.jcis.2025.138721
7. Wu YY, Tian X, Jiang Y, Ma HY, Wang W, Zhang WS, Martin JS, Yan Y, Qin DD, Han DX, Niu L (2024) Advances in bimetallic materials and bimetallic oxide nanozymes: Synthesis, classification, catalytic mechanism and application in analytical chemistry. TrAC Trends Anal Chem 176:117757. https://doi.org/10.1016/j.trac.2024.117757
8. Zhang CY, Wang C, Zhang XM, Yao CY, Zhu L, Chai X, Zhang JX, You SP, Wang YF, Su RX, Qi W (2026) Recent advances in laccase: From molecular characteristics to advanced applications in biocatalysis, immobilization, and nanozymes. J Environ Chem Eng 14:121035. https://doi.org/10.1016/j.jece.2026.121035
9. Fan HZ, Zhang RF, Fan KL, Gao LZ, Yan XY (2024) Exploring the Specificity of Nanozymes. ACS Nano 18:2533–2540. https://doi.org/10.1021/acsnano.3c07680
10. Wang SJ, Bian WY, Xiang HY, Pan JB, Wang XS, Xie AM, Liu J, Zeng HB, Li WJ (2026) Lanthanide metal-organic frameworks encapsulated carbon quantum dots triggered triple fluorescent centers for heavy metal ions detection. Chem Eng J 528:172531. https://doi.org/10.1016/j.cej.2025.172531
11. Luo LJ, Li JM, Bi XY, Jiang PA, Li LB, Qiao GJ, You TY (2024) Engineering three-in-one fluorescent nanozyme of Ce-Au NCs for on-site visual detection of Hg^{2+}. J Hazard Mater 476:134967. https://doi.org/10.1016/j.jhazmat.2024.134967
12. Peng YL, Du KZ, Yue HG, Li H, Li HX, Liu M, Shangguan SH, He XC, Li XX, Chang YX (2026) Integrated deep eutectic system enrichment and AI-assisted high-throughput visual detection for Hg^{2+} in environmental samples. J Adv Res 79:801–817. https://doi.org/10.1016/j.jare.2025.04.011
13. Liu JX, Lin S, Xiang XL, Qi KZ (2026) Construction of S-scheme heterojunction dual-path photocatalytic hydrogen peroxide synthesis by covalent organic frameworks loaded with $AgInS_2$ quantum dots. J Colloid Interface Sci 708:139786. https://doi.org/10.1016/j.jcis.2025.139786
14. Chang LP, Bai YJ, Gao WQ, Han XY, Cheng ZX, Yu JH, Zhu PH (2026) A novel conductive 3D covalent organic framework for high-performance trimethylamine gas sensing at room temperature. J Hazard Mater 503:141104. https://doi.org/10.1016/j.jhazmat.2026.141104
15. Guo XT, Wang XY, Wen SZ, Wu HZ, Wang J, Wang M, He DW, Zhao FQ, Liu JK, Yang XQ, Wang SA (2025) Silver Nanoparticle-Grafted Amidoxime Covalent Organic Framework: A Highly Sensitive and Selective SERS Substrate for Uranium Detection in Natural Water Systems. Adv Funct Mater 35:2500901. https://doi.org/10.1002/adfm.202500901
16. Lei QY, Zou YY, Yan JS, Cheng J, Guo JH, Li DG (2026) Advances and challenges in the application of artificial intelligence to medical biosensing technology: A review. TrAC Trends Anal Chem

195:118592. https://doi.org/10.1016/j.trac.2025.118592

17. Ma HY, Jia L, Li JY, Zhang LN, Li YX, Zhu TF, Xu (2026) Smart three-in-one detection platform: Chemical sensing, image recognition, and machine learning for rapid identification of tetracycline antibiotics. Acta Part Mol Biomol Spectrosc 350:127416. https://doi.org/10.1016/j.saa.2025.127416
18. Li YC, Ji CX, Cui ZW, Feng JX, Zhang L, Liu S, Zhang WT, Ji YW, Shen YZ, Wang JL (2025) Electron Transfer-Tailored D-Band Center to Boost Nanozyme Catalysis for Interpretable Machine Learning-Empowered Intelligent Biosensing. Adv Sci 12:e05712. https://doi.org/10.1002/advs.202505712
19. Zehra F, Fatima T, Khanuja MT (2025) Colorimetric Sensing of Mercury with Machine Learning Based on Nanozyme Activity of Chitosan Functionalized MXene/ZIF-L Nanocomposite. Adv Mater Technol n/a e00519. https://doi.org/10.1002/admt.202500519
20. Ma WD, Li GR, Zhong C, Yang YX, Sun QQ, Ouyang D, Tong W, Tian WC, Zhang L, Lin ZA (2021) Room-temperature controllable synthesis of hierarchically flower-like hollow covalent organic frameworks for brain natriuretic peptide enrichment. Chem Commun 57:7362–7365. https://doi.org/10.1039/D1CC02646A
21. Jia ZX, Shi D, Wang JB, Lin XC (2024) Covalent organic frameworks surface-anchored with silver nanoparticles for colorimetric detection of dopamine based on its oxidase-mimicking activity. Microchem J 200:110428. https://doi.org/10.1016/j.microc.2024.110428
22. Zhang ZY, Liu D, Zhang XS, Luo XL, Lin WM, Li ZH, Huang JH (2023) Silver nanoparticles deposited carbon microspheres nanozyme with enhanced peroxidase-like catalysis for colorimetric detection of Hg^{2+} in seafood. Microchim Acta 190:340. https://doi.org/10.1007/s00604-023-05921-w
23. Wang D, Zhang Y, Li XT, Lei P, Shuang SM, Dong C (2025) The smartphone-assisted sensing platform based on manganese dioxide nanozymes for the specific detection and degradation of hydroquinone. J Hazard Mater 487:137133. https://doi.org/10.1016/j.jhazmat.2025.137133
24. Ma WJ, Mao JJ, He CT, Shao LH, Liu J, Wang M, Yu P, Mao LQ (2022) Highly selective generation of singlet oxygen from dioxygen with atomically dispersed catalysts. Chem Sci 13:5606–5615. https://doi.org/10.1039/D2SC01110G
25. Liu SJ, Liao SC (2021) Surface Modification of Bamboo Charcoal by O_2 Plasma Treatment and UV-Grafted Thermo-Sensitive AgNPs Hydrogel to Improve Antibacterial Properties in Biomedical Application. Nanomaterials 11:2697. https://doi.org/10.3390/nano11102697
26. Zhu GB, Hou JL, Xu J, Li J, Wang CX, Yi YH (2024) Enhanced peroxidase-like activity based on electron transfer between platinum nanoparticles and Ti_3C_2TX MXene nanoribbons coupled smartphone-assisted hydrogel platform for detecting mercury ions. Anal Chim Acta 1329:343250. https://doi.org/10.1016/j.aca.2024.343250
27. Li Y, Tong WS, Li XN, Wang XM, Zhang XX, Li XW, Zhang YH, Xu C (2026) Attapulgite Template for Oxygen Vacancies Boost of Manganese Dioxide Nanozymes With High Oxidase-Like Activity. https://doi.org/10.1002/smll.202512686. Small e12686

Figures

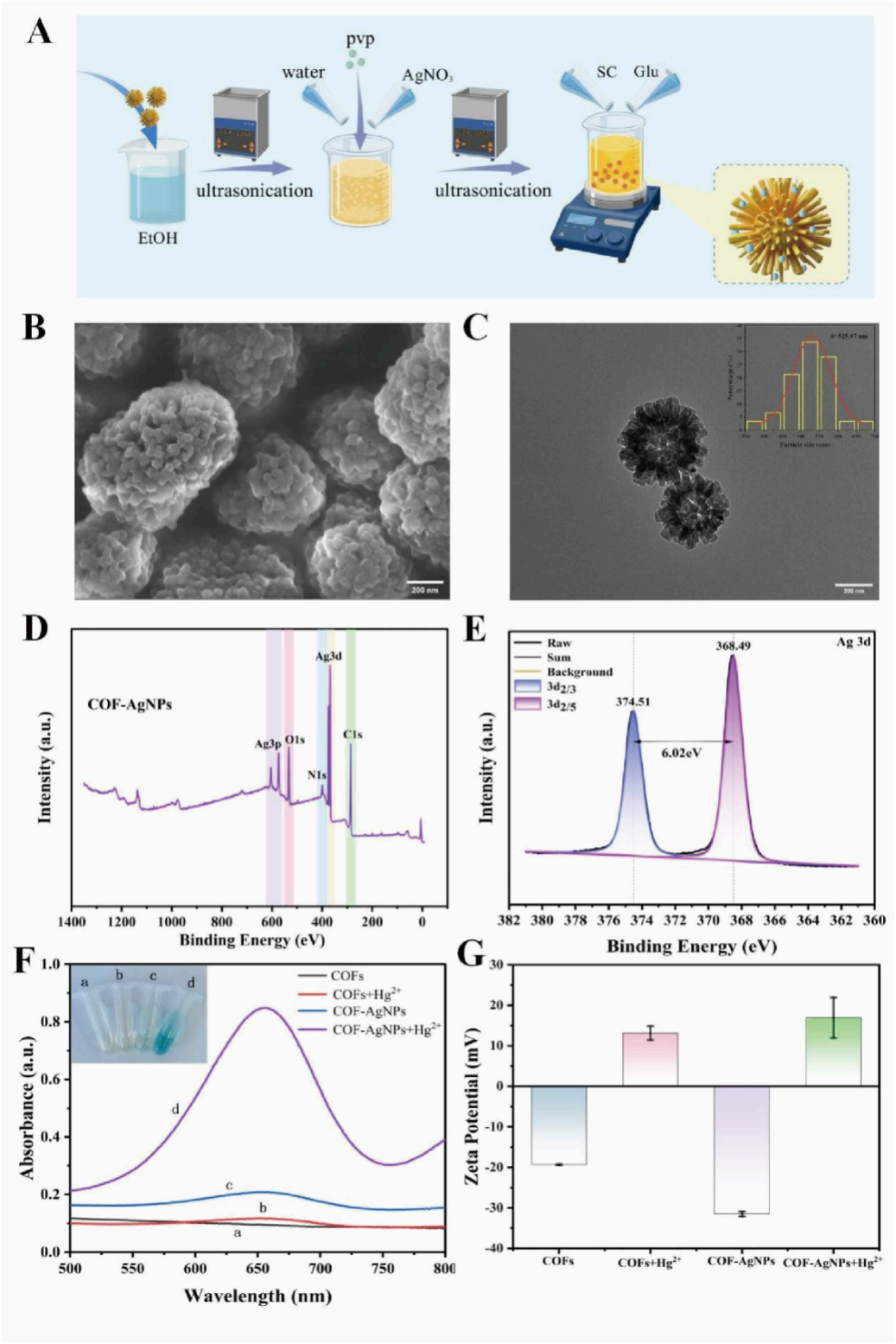


Figure 1

(A) SEM image of COF-AgNPs; (B) TEM image and particle size distribution of COF-AgNPs (inset); (C) XPS full spectra of COF-AgNPs; (D) High-resolution XPS spectra of Ag3d in COF-AgNPs; (E) UV-Vis absorption spectra and corresponding solution photographs of COFs, AgNPs, COF-AgNPs reacted with

TMB in the presence/absence of Hg^{2+} (inset); (F) Zeta potential distribution of COFs, COFs + Hg^{2+}, COF-AgNPs and COF-AgNPs + Hg^{2+}.

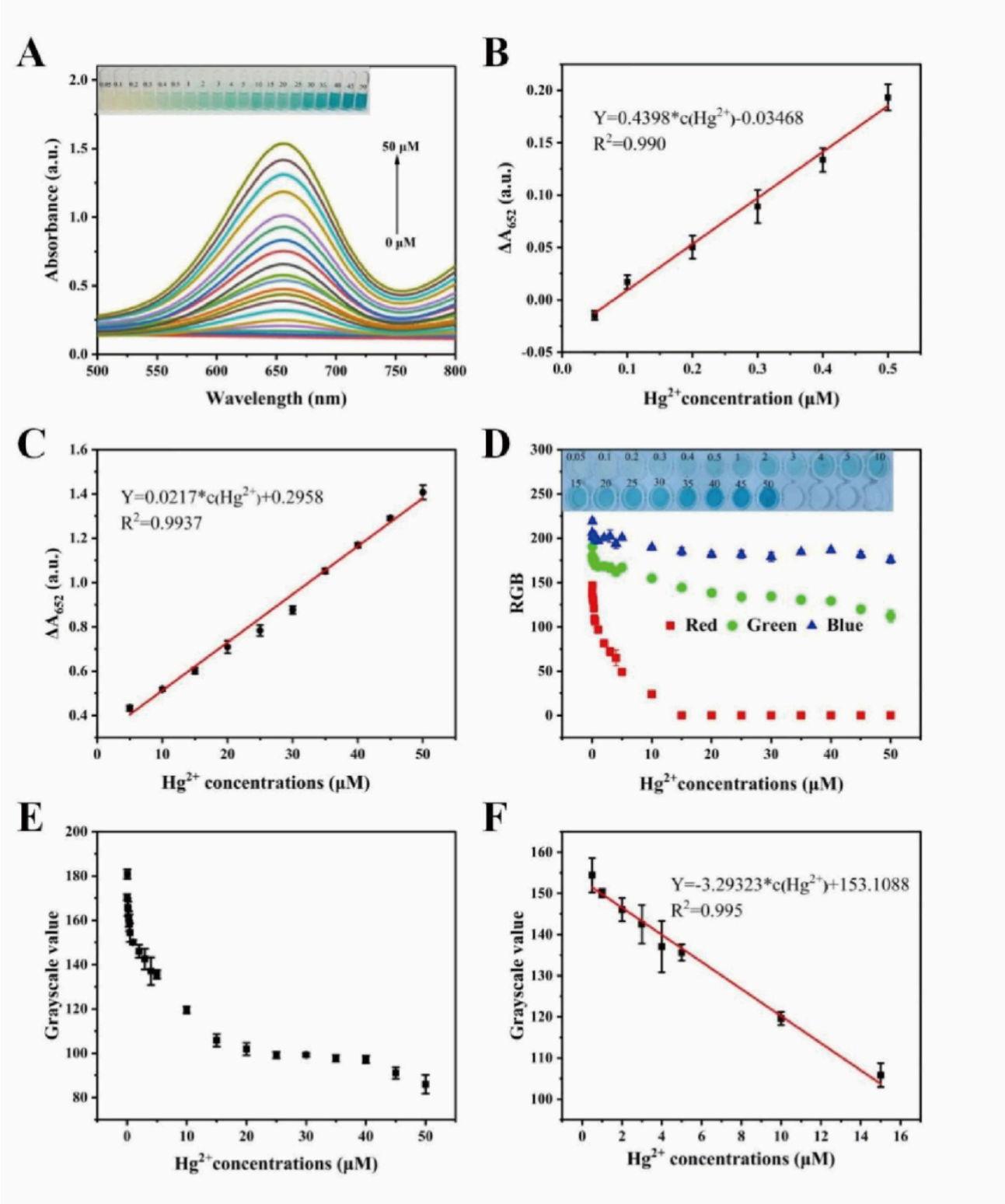


Figure 2

(A) UV-Vis absorption spectra (500-800 nm) as a function of Hg^{2+} concentrations (inset: photographs of the colorimetric reaction); (B) Linear calibration curve for Hg^{2+} detection by microplate reader (linear

range: 0.05-0.5 μM); (C) Linear calibration curve for Hg^{2+} detection by microplate reader (linear range: 5-50 μM); (D) RGB values as a function of Hg^{2+} concentrations obtained by smartphone analysis (inset: photographs of color development); (E) Grayscale intensity profile as a function of Hg^{2+} concentrations; (F) Linear calibration curve for Hg^{2+} detection based on RGB values.

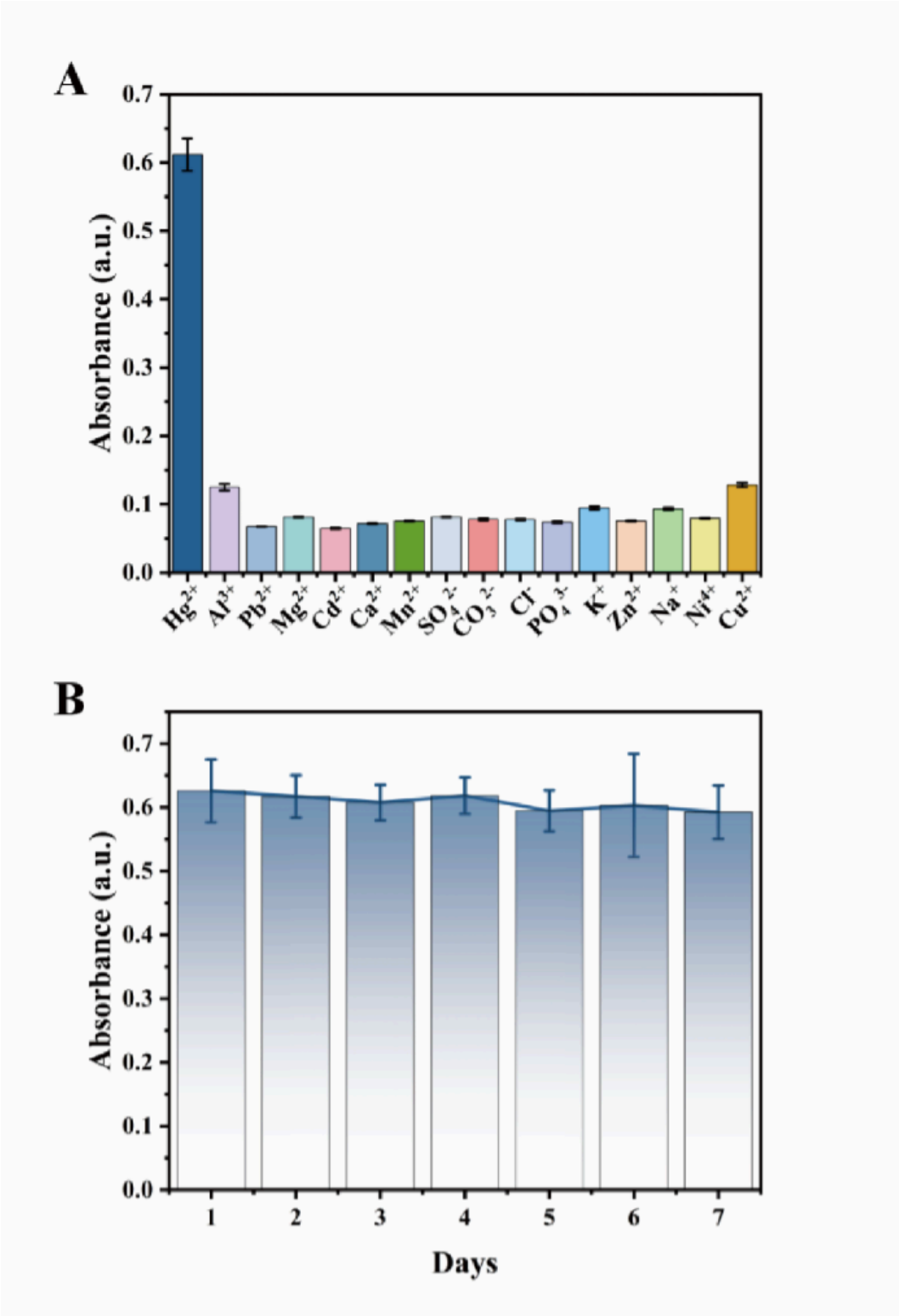


Figure 3

(A) Effects of common metal cations and anions on the absorbance response for Hg^{2+} detection; (B) Time-dependent (7 days) enhancement of oxidase-like activity in COF-AgNPs induced by Hg^{2+}.

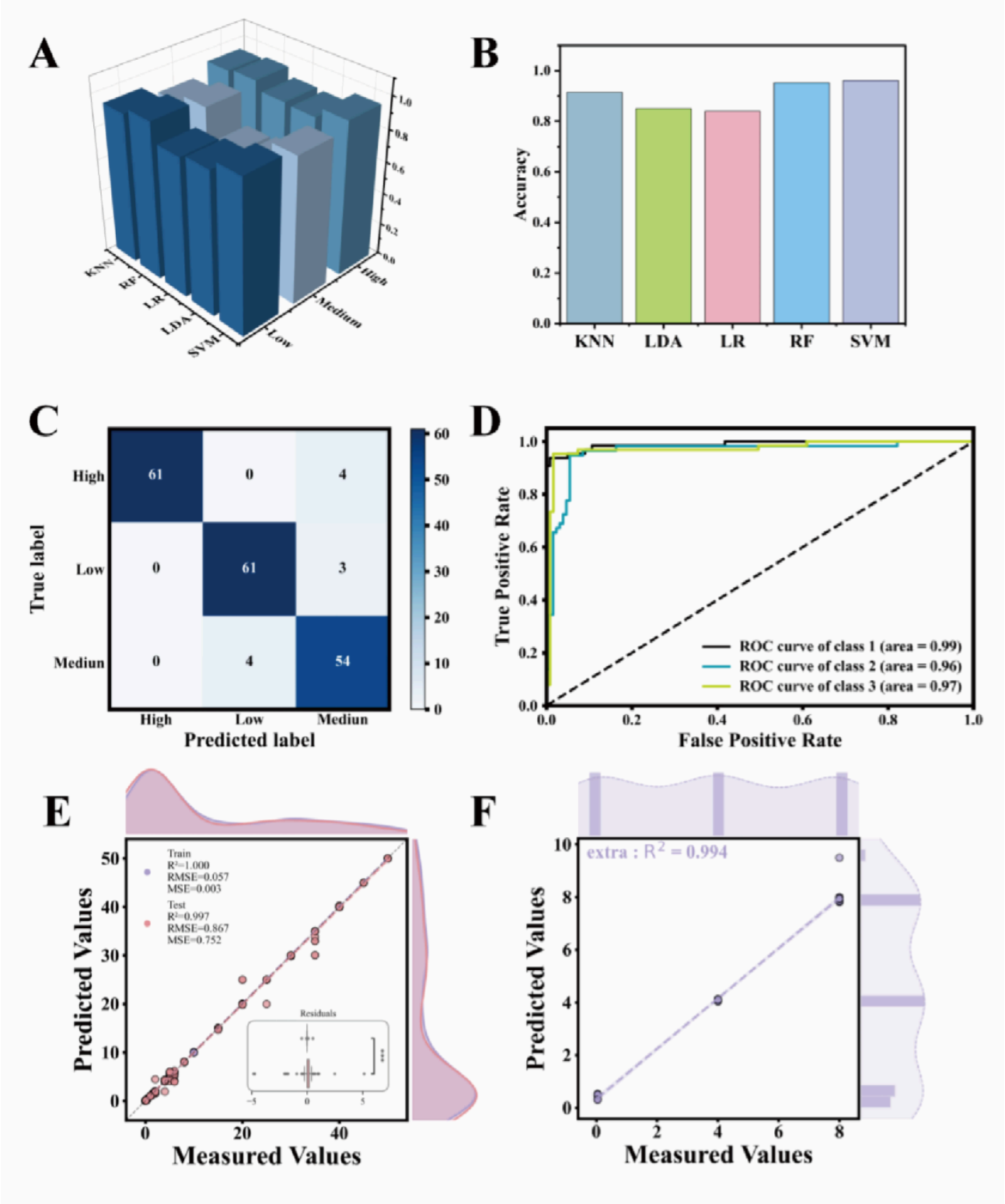


Figure 4

(A) Performance comparison of machine learning models across low, medium, and high concentration ranges; (B) Overall performance benchmarking of ML models; (C) Visualization results of the confusion

matrix for the decision tree model; (D) ROC curve of the decision tree model and corresponding area under the curve (AUC) analysis; (E) Regression scatter plot of the model prediction values versus actual measured values, along with error distribution; (F) Linear regression plot of the model prediction values versus actual measured values in practical samples.

Supplementary Files

This is a list of supplementary files associated with this preprint. Click to download.

- SupplementaryMaterial.docx
- Graphicalabstarct.docx